ACS APPLIED MATERIALS & INTERFACES

Research Article

www.acsami.org

POSS-Enhanced Phase Separation in Air-Processed P3HT:PCBM Bulk Heterojunction Photovoltaic Systems

Qi Wu,[†] Mithun Bhattacharya,[†] and Sarah E. Morgan*

School of Polymers and High Performance Materials, The University of Southern Mississippi, Hattiesburg, Mississippi 39406-5050, United States

Supporting Information

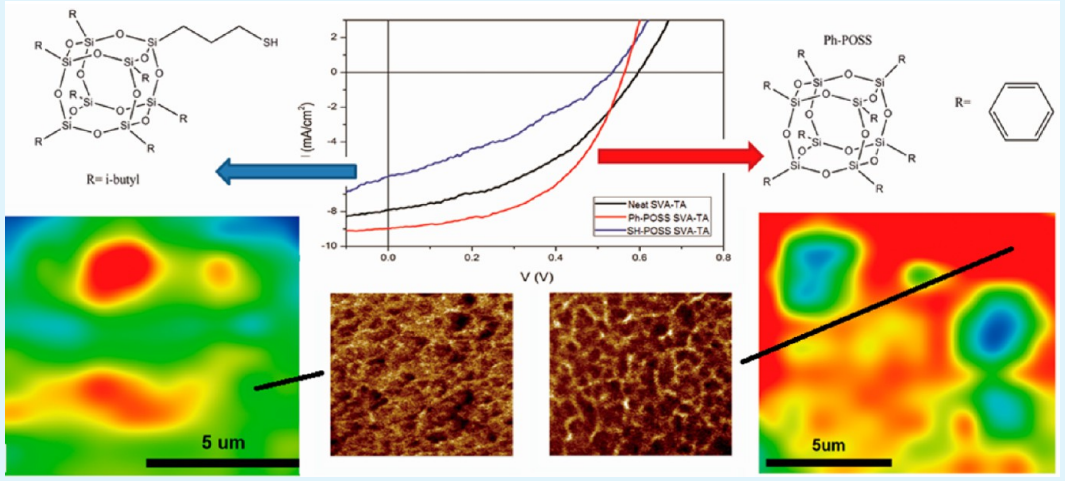

ABSTRACT: Nanoparticles have been shown in some cases to improve phase separation and morphology in bulk heterojunction organic photovoltaic cells. In this study, the effect of incorporation of polyhedral oligomeric silsesquioxane (POSS) molecules of different structures in air processed poly(3-hexylthiophene-2,5-diyl) (P3HT) and [6,6]-phenyl C_{61} butyric acid methyl ester (PCBM) films and photovoltaic cells was evaluated. Morphology and composition of the nanoscalephase-separated domains were determined via conductive atomic force microscopy in conjunction with nanomechanical mapping and Raman imaging. UV−vis and fluorescence spectroscopy analysis of the films was performed at different stages of the process and with different levels of solvent vapor and thermal annealing. It was found that POSS molecules of selected structures provided enhancement in morphology control in films, translating to improvements in fill factor and power conversion efficiency of laboratory-scale OPV cells. The findings indicate the potential for further improvements in solar cell performance with specifically tailored POSS/polymer phase-separated systems.

KEYWORDS: *POSS, photovoltaic, phase separation, morphology, AFM, raman imaging*

1. INTRODUCTION

Polymer-based organic photovoltaic (OPV) devices have attracted considerable attention over the past decade because of their ease of fabrication, low weight, flexibility, and potential reduction in cost.[1] The key disadvantage of OPV cells is their low power conversion efficiency compared with inorganic cells. Power conversion efficiency is determined by the process of photon absorption, exciton separation, and prevention of recombination of electron/hole pairs prior to collection at the electrode, which is determined in turn by the composition and morphology of the phase-separated active layer in the OPV device. The active layer typically consists of a p-type conjugated polymer, which serves as the donor, and an n-type fullerene derivative, which serves as the acceptor. On absorption of light energy, an exciton is generated, which undergoes charge separation after diffusion to the donor/acceptor interface. The degree of phase separation, the size of thephase-separated domains, and the organization of the domains determine the charge diffusion pathways and recombination processes. It has been reported that the highest conversion efficiency is achieved when the domain size is equal to the exciton diffusion length.[2,3] Phase separation is generally achieved through control of the crystallization and aggregation processes of the donor and acceptor components, respectively. Processing techniques including thermal,[4−6] solvent,[7] and solvent vapor annealing[8] have been reported to enhance phase separation.[11,12]

A typical air processed photovoltaic cell consists of an anode layer, hole transporting layer, active layer and cathode layer. For

Received: March 22, 2013
Accepted: June 10, 2013
Published: June 10, 2013

   dx.doi.org/10.1021/am4010489 | ACS Appl. Mater. Interfaces 2013, 5, 6136−6146

such a device with P3HTand PCBM, the power conversion efficiency is 2.2%, when processed in air.[9] Higher efficiencies can be achieved by inserting an interfacial electron transport layer and when processing under inert conditions; however, this is an obstacle for large scale industrial production.

Studies have been reported of incorporation of nanoparticles, including carbon nanotubes,[10] silver nanowires,[11] and gold nanoparticles,[12] in the active layer in an attempt to enhance morphology control. However, difficulty in obtaining adequate dispersion of the nanoparticles in the polymer blend limits their beneficial effects on the OPV system.

POSS nanostructured chemicals are hybrid organic−inorganic structures, monodisperse in size, consisting of a silicon oxide cage with a corona of organic substituents. By varying the organic groups, it has been shown that the migration and aggregation behavior of POSS molecules can be controlled in polymeric matrices to produce desired nanostructure development with associated performance improvements,[13−15] and POSS molecules can be tailored to serve as dispersing agents for organic and metallic nanoparticles.[16,17] It is also possible to effect changes in the morphology, crystallinity and phase dispersion in polymeric blend systems on incorporation of specific POSS systems.[18,19] It has been reported that POSS molecules facilitate the electron injection and promote current density when attached to semiconducting polymers.[20,21] To the best of our knowledge, a study of POSS performance in OPV films has not yet been reported.

Polydimethylsiloxane (PDMS), a linear, long-chain macromolecule with siloxane backbone structure similar to that of the POSS cage, was evaluated by Graham et al. in a low band gap polymer blend. They reported that addition of PDMS increased J_{sc} by 50% and efficiency by 70% over the low-efficiency control.[22] PDMS is not as easily functionalized as POSS to provide compatibility with the active layer, and, as it is a flexible, long-chain molecule, it is not expected to provide structural rigidity to the blend. Small molecule additives with better miscibility than PDMS also have been used to improve the performance of organic photovoltaic cells by controlling the ternary morphology during the solvent evaporation process.[23−25] However, unlike the rigid POSS molecules, they are removed during solvent evaporation and cannot impart additional structural rigidity to the blend after drying.

Although incorporation of nanoparticles may result in enhanced OPV performance, development of a full understanding of the nanoscale morphology and mechanism of action in these complex blends is challenging. Raman imaging has been utilized to distinguish the donor and acceptor domains on the micrometer scale;[26,27] however, it does not have the resolution to determine nanoscale morphology. Atomic force microscopy (AFM) provides resolution of less than 10 nm in evaluating surface features of polymeric films. Traditional AFM tapping mode evaluation is widely used in morphology characterization; however, it is difficult to extract compositional information of phase-separated systems on the basis of only the height and phase images. Recently developed nanomechanical mapping AFM modules have become available in which it is possible to simultaneously extract topographical and materials properties information, including relative surface hardness, modulus, and adhesion, at each point using a calibrated probe with known parameters.[28,29] Conductive AFM (C-AFM) techniques allow further determination of the composition of phase-separated OPV blends, where the hole and electron pathways can be identified at the nanoscale using current mapping analysis.[30]

In this study, POSS molecules were first introduced into an air processed P3HT and PCBM OPV system. Two types of POSS molecules with different functional groups were chosen to explore the effects of POSS interaction with blend components. Films were analyzed at different stages of the pre- and postannealing processes of the active photovoltaic layer, and the relationship between morphology and composition was studied by nanomechanical mapping, conductive AFM, spectroscopic studies, and Raman imaging. The effects of POSS-induced morphology and absorbance changes on OPV device performance were determined.

2. EXPERIMENTAL SECTION

Materials. Unpatterned indium tin oxide (ITO) glass slides with 8−12 Ω/sq resistance were purchased from Sigma Aldrich. Patterned ITO coated glass slides with coating thickness ∼100 nm and surface resistivity of 8−12 Ω/sq were purchased from Luminescence Technology Corp., to use as the transparent anode. Poly(3,4-ethylenedioxythiophene)-poly(styrenesulfonate) (PEDOT-PSS), obtained from Ossilla as a 1.3 wt % dispersion in water having resistivity in the range of 500−5000 Ω cm, was used as the hole transporter. P3HT, electronic grade, 98% regioregular, 99.995% pure on trace metals basis, average $M_n \approx 45\,000$, was obtained from Sigma Aldrich. PCBM obtained from Sigma Aldrich with purity >99% and molecular weight of 911 g/mol was used as the acceptor. Octaphenyl POSS (Ph-POSS) and mercaptopropylisobutyl POSS (SH-POSS) with 99% purity were provided by Hybrid Plastics, Inc. *o*-Dichlorobenzene (DCB) from Acros was used as the solvent to form the actual photovoltaic donor/acceptor blend. For solvent vapor annealing (SVA), isopropanol (IPA) was used. All the materials were used as received.

Sample Preparation. *Photoactive Films for Spectroscopic and Microscopic Analysis (without cathode layer).* The photoactive P3HT:PCBM blend (ratio 1:0.6) was prepared in DCB (25 mg/mL) in an amber vial. The mixture was heated at 60 °C for 1 hto promote dissolution and then subjected to gradient cooling to room temperature in the same oil bath. It was then kept at room temperature for 24 h. The POSS-modified samples were prepared by adding 1 wt % Ph-POSS or 1 wt % SH-POSS to the initial P3HT:PCBM mixture. POSS concentration was held at 1 wt % based on preliminary screening studies indicating optimum device performance at this level. ITO (∼100 nm)-coated glass plates were successively cleaned ultrasonically in deionized water, acetone and IPA for 10 min each. They were dried under N_2 and exposed to UV/ozone for 40 min and then immediately spin-coated with a uniform layer of PEDOT:PSS. The PEDOT:PSS dispersion was spin-coated at a speed of 5000 rpm for 2 min. The PEDOT:PSS-coated substrates were then dried for 15 min on a hot plate at 150 °C in air, which was measured by AFM to be 40 ± 5 nm thickness. The P3HT:PCBM blend solution was spin-coated on top of the PEDOT-PSS layer at 1250 rpm for 70 s. The thickness of such active layers was found to be 100 ± 10 nm, as measured using AFM scratch testing. Solvent vapor annealing was performed for 20 min in a chamber saturated with IPA vapor. The samples were then thermally annealed at 150 °C in argon for 30 min. The entire fabrication process was conducted in an air environment except for the thermal annealing (TA) step. The above samples prepared on unpatterned ITO glass were further studied by optical microscopy, AFM, Raman imaging, UV−vis spectroscopy and fluorescence spectroscopy. Two annealing processes were conducted in this study, one involving only solvent vapor annealing (SVA) and the other using both SVA and thermal annealing (SVA-TA).

Solar Cells for Analysis of Power Conversion Efficiency (with 100 nm coating of aluminum to form the cathode). The devices for performance measurement were prepared on patterned ITO glass. The glass cleaning process was the same as that used for the unpatterned ITO glass. After exposure to UV/ozone for 40 min, the ITO glass was

spin coated with the PEDOT:PSS dispersion at a speed of 5000 rpm for 2 min. Then the slides were heated on a hot plate at 150 °C in air for 15 min. The P3HT:PCBM (ratio 1:0.6) photoactive blend (the same composition as described previously for microscopic analysis) was spin coated on the baked PEDOT:PSS layer, then subjected to 20 min of solvent vapor annealing in an IPA saturated chamber, and then a 100 nm thick layer of Al (cathode) was evaporated on top of the active layer through a shadow mask using metal evaporation function by a Q150T Turbo-Pumped Sputter Coater. The deposition rate was controlled to 35 nm/min to achieve reproducible coatings and device performance. The solar cells thus formed were then annealed at 150 °C in argon for 30 min. Three identical devices were made and each device had six cells, with an active area of 0.042 cm^2.

Analytical Techniques. The optical microscopy images were obtained using a VHX digital microscope from Keyence. For this study, all images were collected at a magnification of 1000X .

Raman images were collected with a DXR Raman Microscope from ThermoScientific. A laser beam of 532 nm was focused with a 100×/0.95 objective in the optical microscope. The laser power was 5 mW and the aperture was a 25 μm pinhole. The autofocus function was employed during the scanning to ensure that the laser was focused on the surface of the film. All images were baseline corrected. The resolution of the images is 540 nm.

AFM studies were conducted on a Dimension ICON scanning probe microscope from Bruker. The nanomechanical mapping images were acquired after calibration of the probe. A silicon probe from Bruker (RTESP) with nominal spring constant of 20−80 N/m was employed. The calibration process followed the absolute method and was checked through the relative method, which is suggested by the supplier. After calibration of the AFM tip, the elastic modulus of the surface is estimated from the slope of the force-displacement curve when the tip is in contact with the surface, following Derajaguin−Mueller−Toporov (DMT) theory. This is known as the DMT modulus[31−33] The evaluation of the DMT modulus was carried out using the Nanoscope Analysis 1.40 software, Bruker. All the processes were performed in the peakforce QNM air mode in Nanoscope 8 software. First a standard sapphire sample from Bruker was scanned and a force curve was obtained. The deflection sensitivity was calculated from the force curve using the software. Three different positions were chosen to ensure consistency of measurements. The average value was then used as the final deflection sensitivity. After obtaining the deflection sensitivity, the probe was withdrawn from the surface. Thermal tune function in the software was performed to obtain the resonance frequency of the probe, through which the spring constant was calculated. A standard titanium sample from Bruker and a neat P3HT:PCBM sample were then scanned with the previous parameters. The tip radius was calculated from the deformation image of the Ti sample and the height image of the neat P3HT:PCBM sample through the Nanoscope Analysis software. Finally a standard PEG-PS reference sample from Bruker was tested to make sure the expected elastic modulus value was obtained. A value of 0.3 was used as an estimate for Poisson's ratio and the scan rate was held at 1 Hz during the measurements. The height image and corresponding modulus image were obtained during one single scan. The root-mean-square (RMS) value from the height image was utilized to characterize the roughness of the surface. The average modulus value of the modulus image was used to show the stiffness of the surface. For those images with large (>1 μm) phase-separated features, the modulus values were calculated on the basis of the flat areas, which exclude the micrometer-scale features.

The conductive AFM analysis was performed using a probe from Bruker (SCM-PIC) with a thin platinum/iridium front side coating. The nominal spring constant of the probe was 0.18−0.42 N/m. Tip radius of the probe was 8 nm. During scanning, a bias of +2 V was applied between the ITO layer and the AFM probe. Both height images and corresponding current images were obtained during the measurements. Since the height images in C-AFM are similar to those obtained in nanomechanical mapping, only current images are shown. In calculations of average current, the micrometer-sizedphase-separated features were excluded in those images where they were present.

Fluorescence spectra were obtained using a TECAN Infinite M1000 microplate reader with premium Quad4 monochromators. UV−vis spectra were obtained using a Perkin-Elmer Lambda 6 UV/vis spectrophotometer. The spectra normalization was carried out at 700 nm, where there is negligible absorption by the blend components. It was so chosen to identify the effect of each component (P3HT and PCBM) independently.

UV−vis and XRD analyses were preformed immediately after completion of the annealing procedure. AFM imaging was performed on the same day, while Raman and fluorescence studies were performed within two days of processing to standardize the time between processing and characterization. In each case, the three types of samples (neat, Ph-POSS, and SH-POSS) were produced and evaluated together.

Current−voltage (J−V) measurements were carried out using a Keithley 2400 source unit. Irradiation was provided by an AM1.5 solar simulator (Photo Emission Tech. Inc.) with illumination of 1000 W/m^2 from a Xenon lamp coupled to a monochromator. The total incident light intensity was calibrated with a standard reference silicon solar cell.

3. RESULTS AND DISCUSSION

It is well-known that processing conditions, including thermal and solvent vapor annealing, affect nanoscale morphology and conversion efficiency in P3HT/PCBM OPV systems.[34] For the current study, a protocol was determined that reproducibly yielded the highest conversion efficiencies in air-processed OPV cells produced in our laboratories (results reported previously).[35] It was found that cells produced with a 20 min IPA solvent vapor annealing step followed by a 30 min thermal annealing step at 150 °C yielded the best performance. The choice of solvent for solvent vapor annealing was governed by two parameters − the solubility parameter and the boiling point. We previously demonstrated that during solvent vapor annealing of partly wet thin films, the use of a nonsolvent resulted in a more favorable self-assembly of the polymer than that produced with a good solvent.[35]A good solvent increased the phase domain sizes beyond desirable limits. So a solvent (IPA[36]) with solubility parameter close to that of PCBM[37] but farther from that of P3HT[38] was chosen. This facilitated greater PCBM mobility, thereby initiating favorable PCBM aggregation even before the thermal annealing step. Also, the choice of a low boiling solvent ensured greater and faster penetration through the cross-section of the film, resulting in efficient donor−acceptor assemblies. Similar concepts have been utilized earlier.[39]. In an attempt to further optimize the morphology of the active layer, two types of POSS were introduced into the P3HT:PCBM system separately, whose structures are shown in Scheme 1. The POSS structures were chosen for their potential interactions with the phase-separated domains, where Ph-POSS is expected to have greater affinity for the PCBM phase and SH-POSS for the P3HT phase. Spectroscopy and microscopy analyses were performed on multilayer photoactive films without the cathode layer, whereas solar cell performance studies were performed on cells with an Al cathode layer coating.

Optical Microscopy. Figure 1 shows the optical microscopy images of the OPV blends with and without POSS. The neat OPV film appears uniform and smooth (Figure 1A). In the Ph-POSS-modified film (Figure 1B), oblong features 1−3 μm in diameter are observed which are attributed to POSS/polymer clusters. A smaller number of widely distributed oblong features are observed in the SH-POSS-modified film

Scheme 1. Structures of SH-POSS and Ph-POSS

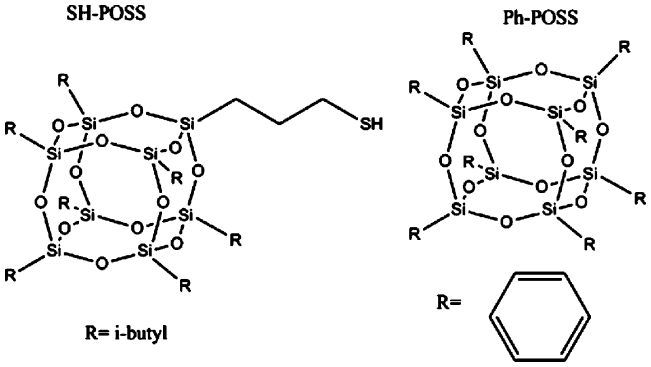

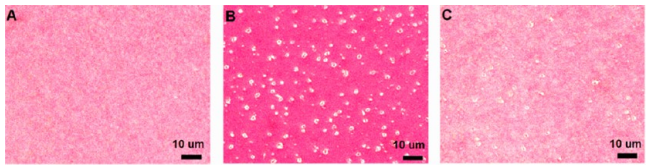

Figure 1. Optical microscopy images (1000×) of (A) the neat P3HT:PCBM film, (B) the Ph-POSS-modified film, and (C) the SH-POSS-modified film after SVA-TA. POSS is incorporated at 1 wt %.

(Figure 1C). The morphology variations in the samples arise from the different functional groups on the POSS molecules, as discussed in the following sections.

Raman Imaging. Raman imaging analysis was performed to gain information about the compositions of the clusters observed in the Ph-POSS and SH-POSS-modified films observed by optical microscopy. The Raman spectrum of the neat film was obtained to provide baseline information (Figure 2). The peak at 1447 cm^{-1} is attributed to the symmetric C═C stretch and the peak at 1325 cm^{-1} is attributed to the C−C intraring stretch of P3HT.[40,41] Because of the high intensity of the P3HT bands (related to the high crystallinity and close packing of the P3HT phase), the much lower intensity PCBM bands are difficult to discern. Thus, in accordance with previous literature reports,[2] the high intensity peak at 1447 cm^{-1} was used to determine the distribution of P3HT in the films.

Raman imaging maps of the 1447 cm^{-1} peak are shown in Figure 3 for the neat P3HT:PCBM film (a), the Ph-POSS-modified film (b), and the SH-POSS-modified film (c). The neat OPV film shows nearly uniform peak intensity, indicating uniform P3HT concentration distribution at the resolution of the Raman imaging (540 nm). Images b and c in Figure 3 show wide variations in peak intensity, with the red domains representing highest peak intensity and thus highest relative P3HT concentration, and the blue domains representing lowest P3HT concentration. The Ph-POSS-modified film (Figure 3b) shows micrometer-sized, oblong, low-intensity features that are attributed to domains with low P3HT concentration. The SH-POSS-modified film (Figure 3c), in contrast, shows high intensity oblong features that are attributed to domains with high P3HT concentration.

AFM Analysis. Nanomechanical mapping allows simultaneous analysis of surface topography and mechanical properties of the film surface. Utilizing a calibrated probe with known physical parameters, it is possible to determine relative hardness and stiffness of nanoscale-separated features on the surface, and thus infer the composition of the phase-separated morphological features. Figure 4 shows comparative height (1), DMT modulus (2), and current (3) images for the three P3HT:PCBM films, neat (A), Ph-POSS-modified (B), and SH-POSS-modified (C). Physical parameters measured for the films are given in Table 1. The neat P3HT:PCBM film displays the nanoscaled phase-separated morphology typically observed for this system. The bright spots (approximately 20 nm in diameter) apparent in the AFM DMT modulus image correspond to the bright spots in the C-AFM image for the P3HT:PCBM film (A2 and A3, respectively), AFM analysis of neat PCBM and P3HT films showed that PCBM DMT modulus was 1 order of magnitude higher and PCBM conductivity 2 orders of magnitude higher than that measured for P3HT (Table 1). Under positive bias, electrons flow from the AFM tip to the surface, and the PCBM electron acceptor phase is expected to show higher conductivity and appear brighter in the C-AFM images.[42] The bright features in the neat PCBM:P3HT DMT modulus and C-AFM images are therefore attributed to the PCBM phase. The POSS-modified films show quite different morphologies, with large (1 μm in size), bright,

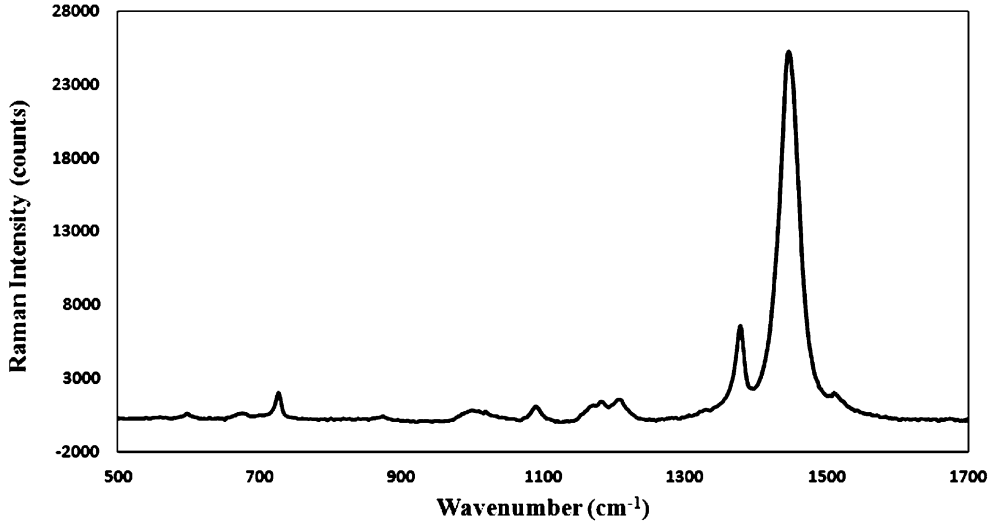

Figure 2. Raman spectrum of the neat P3HT:PCBM film after SVA-TA.

dx.doi.org/10.1021/am4010489 | ACS Appl. Mater. Interfaces 2013, 5, 6136−6146

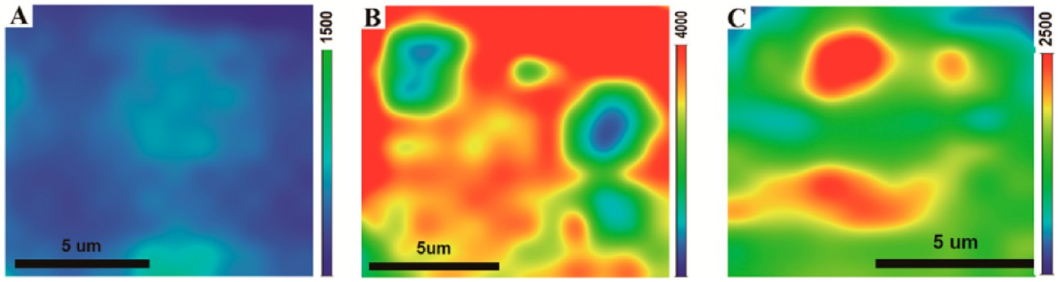

Figure 3. Raman images of the (A) neat P3HT:PCBM film, (B) Ph-POSS-modified film, and (C) SH-POSS-modified film after SVA-TA. The color bar indicates the peak intensity at 1447 cm^{-1}.

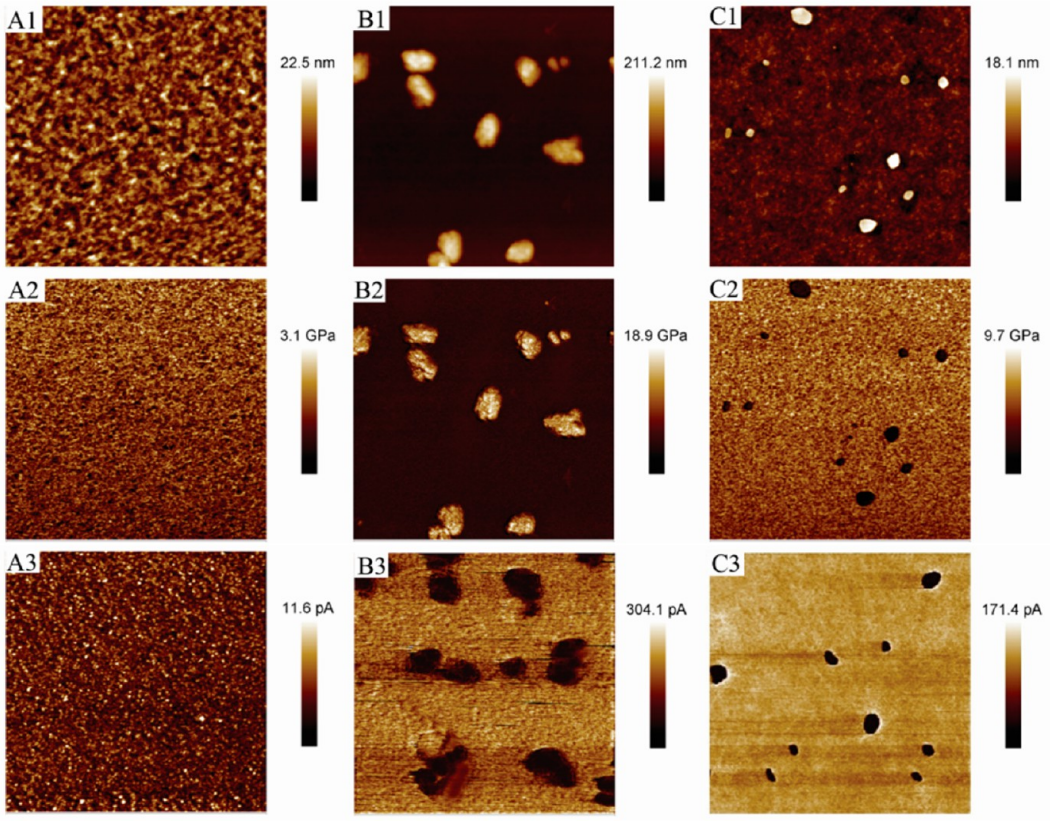

Figure 4. (A1) Height image, (A2) corresponding DMT modulus image, and (A3) current image of P3HT:PCBM film after SVA-TA; (B1) height image, (B2) corresponding DMT modulus image, and (B3) current image of the Ph-POSS-modified film after SVA-TA; (C1) height image, (C2) corresponding DMT modulus image and (C3) current image of the SH-POSS-modified film after SVA-TA. The lateral dimensions of all images are 5 μm × 5 μm.

oblong features apparent in the height images (B1 and C1). For the Ph-POSS-modified film, corresponding bright features are observed in the DMT modulus image (B2), indicating that the raised features observed in the height images have higher DMT modulus than that of the surrounding material. For the SH-POSS-modified film, however, the oblong features appear darker in the DMT modulus image (C2), indicating that they are lower in relative DMT modulus than the surrounding phase. As determined from cross sectional analysis of the topographic images, the raised features in the Ph-POSS-modified film range from 100−150 nm in height while those in the SH-POSS are 10−20 nm in height.

AFM cross-sectional DMT modulus and conductivity analyses were performed in order to obtain more information about the composition of the raised features observed in the height images of the POSS-containing blends (Figure 5). The baseline information of the individual components listed in Table 1 indicates that the polymeric P3HT shows relatively lower DMT modulus (2.2 GPa) than that of the carbon supported PCBM (11 GPa) and silicon−oxygen supported POSS (15 GPa). The average DMT modulus of the Ph-POSS-modified film excluding the raised areas is 5.3 GPa, whereas the average DMT modulus of the raised features is greater than 10 GPa (Figure 5A1). This indicates that the raised areas consist of clusters of POSS and/or PCBM, while the surrounding phase is a blend with the softer P3HT. For the SH-POSS-modified film, in contrast, the raised areas show lower DMT modulus than the surrounding matrix, indicating that the clusters are high in P3HT content. The surrounding matrix has higher modulus than that of the Ph-POSS film because it is enriched in PCBM. The C-AFM images of both POSS-modified films show that the clusters are lower in conductivity (darker) than the surrounding

Table 1. Nanomechanical and Conductive Properties of Individual Blend Components and OPV Films at Different Stages of Processing[a]

sample	RMS (nm)	DMT modulus (GPa)	average current (pA)
neat P3HT	N/A	2.2	25
neat PCBM	N/A	11.0	1730
neat Ph-POSS	N/A	15.0	N/A
neat SH-POSS	N/A	15.0	N/A
P3HT:PCBM SVA	0.4	5.6	47
P3HT:PCBM SVA-TA	2.7	3.9	4
Ph-POSS SVA	0.5	6.5	248
Ph-POSS SVA-TA	1.1	5.3	112
SH-POSS SVA	0.5	11.4	75
SH-POSS SVA-TA	1.0	9.6	63

[a]Numbers are collected from AFM images excluding micrometer-size phase-separated features.

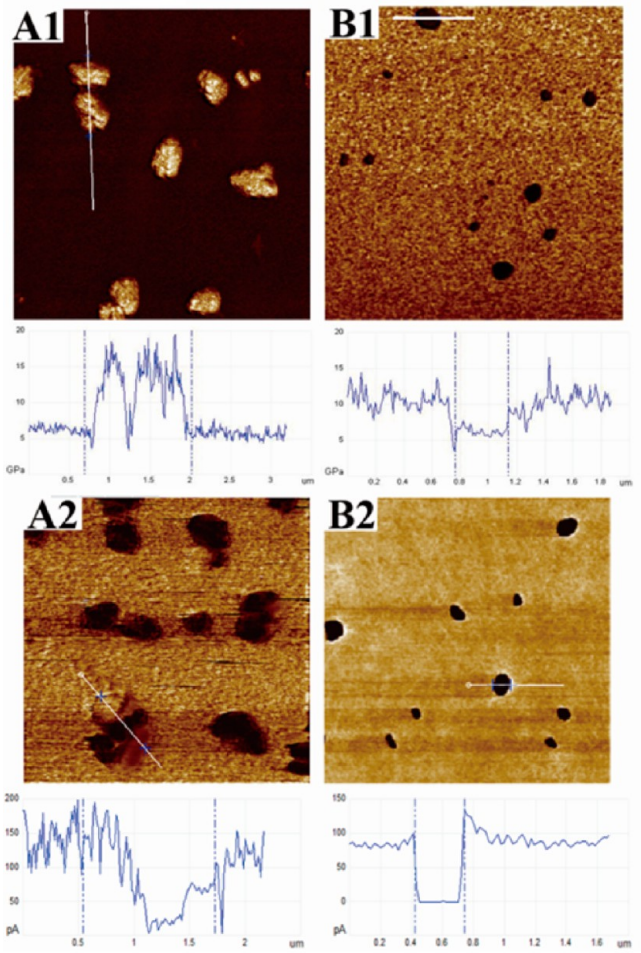

Figure 5. AFM cross-section curves of POSS-modified films after SVA-TA. Ph-POSS: (A1) DMT modulus image and (A2) current image; SH-POSS: (B1) DMT modulus image and (B2) current image. White line indicates cross-section analyzed. The scale of all images is 5 μm × 5 μm.

matrix (Figure 4B3, C3). This indicates that the clusters have a high content of the nonconducting POSS molecules. The cross-sectional analysis of the C-AFM images indicate that there is limited conductivity in the clusters found in the Ph-POSS-modified film (Figure 5A2), but no measurable conductivity in the clusters in the SH-POSS-modified film (Figure 5B2). The combined AFM mechanical and conductivity analyses indicate that the raised features observed in the Ph-POSS-modified films consist of clusters of Ph-POSS with the highly conductive PCBM, whereas the features observed in the SH-POSS-modified film consist of clusters of SH-POSS with P3HT. These findings are consistent with the conclusions from the Raman imaging analysis of the micrometer-sized phase-separated features.

The POSS aggregates observed in Figure 4B protrude from the surface more than 200 nm, and are thus of much greater height than thephase-separated P3HT/PCBM blend component (maximum height approximately 20 nm). With such a great disparity in the height of the topographical features, it is not possible to simultaneously obtain high resolution of the two planes, POSS surface and active layer surface, in the same image. Thus, to evaluate the nanoscale morphology of the blends, AFM images were obtained of 500 nm flat areas in between the raised POSS clusters (Figure 6). Figure 6 A1−C1 shows the 5 μm × 5 μm DMT modulus images, with Figure 6A2−C2 providing corresponding DMT modulus and Figure 6A3−C3 providing corresponding height images from the 500 nm × 500 nm flat areas. Phase-separated polymer domains of 10−20 nm, close to the size of the exciton diffusion length,[2] are observed in the DMT modulus images. The bright features are attributed to the higher modulus PCBM phase and the darker regions to the softer P3HT phase. The Ph-POSS-modified film exhibits the most regular morphology, with a clear network of fiberlike features surrounding evenly spaced softer features. The SH-POSS film shows a higher average DMT modulus, as was observed in the larger scale images in Figure 5, because of enrichment of PCBM in the matrix surrounding the SH-POSS clusters.[43]

To gain a better understanding of the interactions between the POSS molecules and the components of the photoactive polymers, we conducted a study of the effects of processing conditions. Films were prepared using only SVA and both SVA and TA. Nanomechanical mapping and C-AFM images of the POSS-modified films produced with SVA only are shown in Figure 7. The Ph-POSS-modified film after SVA shows a morphology similar to that of the neat OPV film, with a smooth surface and no aggregates. The corresponding SH-POSS-modified film, on the other hand, displays aggregates with low DMT modulus and conductivity, similar to those observed after SVA-TA. Therefore, it is believed that the PCBM/Ph-POSS aggregates are formed during the TA step and the P3HT/SH-POSS aggregates are shaped during the SVA process. This is in accord with previous reports that suggest SVA aides P3HT self-assembly and TA has a more dominant effect on the PCBM aggregation.[35,44] The differences in aggregate formation and composition are attributed to differences in the POSS molecule interactions with the P3HT/PCBM matrix. It is expected that the phenyl substituted Ph-POSS molecules preferentially interact with the PCBM phase through $\pi-\pi$ interactions,[45] and Ph-POSS/PCBM aggregates are formed only after thermal annealing. The SH-POSS molecules are expected to form dimers through thiol coupling reactions when exposed to air,[46] and most likely serve as nucleation sites for P3HT crystallization during the SVA process, resulting in the observed SH-POSS/P3HT aggregates.

The average roughness, DMT modulus and current values collected from AFM images of samples prepared with only SVA

dx.doi.org/10.1021/am4010489 | ACS Appl. Mater. Interfaces 2013, 5, 6136−6146

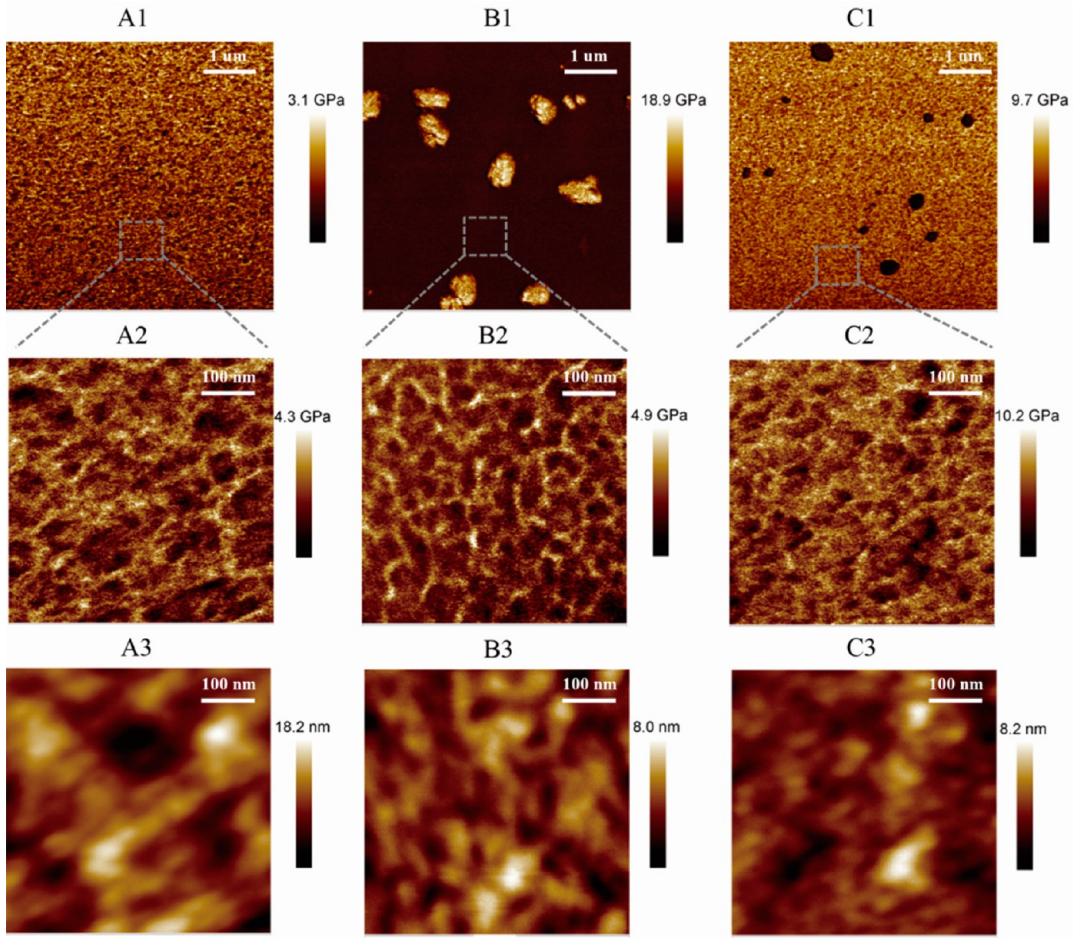

Figure 6. (A1) 5 × 5 μm DMT modulus image, (A2) 500 × 500 nm DMT modulus image, and (A3) corresponding 500 × 500 nm height image of the P3HT:PCBM film after SVA-TA; (B1) 5 × 5 μm DMT modulus image, (B2) 500 × 500 nm DMT modulus, and (B3) corresponding 500 × 500 nm height image of the Ph-POSS-modified P3HT:PCBM film after SVA-TA; (C1) 5 × 5 μm DMT modulus image, (C2) 500 × 500 nm DMT modulus image, and (C3) corresponding 500 × 500 nm height image of the SH-POSS-modified P3HT:PCBM film after SVA-TA.

and both SVA-TA are listed in Table 1. RMS roughness is slightly increased after TA, while DMT modulus and conductivity are slightly decreased. During the thermal annealing process, the amorphous P3HT content decreases as a highly crystalline P3HT phase with finer crystal structure emerges. Similar redistribution of the amorphous and distributed PCBM molecules into well-packed aggregates also ensues. The increases in P3HT crystallinity and PCBM aggregation accompany a small increase in the measured RMS roughness after the TA step. At the same time, a small decrease in the measured DMT modulus and conductivity is observed. We attribute these findings also to the redistribution and restructuring of the amorphous domains into finer crystalline domains, which results in an increase in interfacial material. Rather than being dominated by the peak values obtained from distributed PCBM molecules, the measured values of DMT modulus and conductivity represent an average of the overall contribution of thephase-separated material and interfacial material. Thus, both increased phase separation and a greater distribution of finer structures are expected and desirable changes in morphology, and both correspond to improvements in solar cell performance.

The absorption spectra of the neat P3HT:PCBM and POSS-modified films, with SVA and SVA-TA, are shown in Figure 8. It was found that for all of the films, the absorbance increased after TA. Neat POSS samples showed no absorption in the 350−700 nm range (see the Supporting Information, Figure S1, and previous reports[47]), and thus the increments are attributed to increased crystallinity and packing of the P3HT phase.[48] Remarkably, absorption almost doubles for the Ph-POSS-modified film after thermal annealing. This is attributed to the formation of PCBM-rich clusters during thermal annealing, which enhances phase separation and allows the P3HT to undergo further crystallization. At the same time, the PCBM/POSS clusters play an important role as scattering vectors, which reflect and scatter the light into the film. Such scattering results in increases in the path length traversed by light inside the active layer leading to enhancement of net absorption. We suggest that the PCBM/POSS clusters act in a similar way as the light entrapment features in inorganic solar cells, which can increase the performance greatly.[49]

Fluorescence Study. P3HT fluorescence in the range of 600 and 800 nm is quenched when it is blended with PCBM, due to charge transfer between the molecules.[50,51] Thus the fluorescence quenching intensity is related to the efficiency of charge separation in the OPV film. Figure 9 shows the fluorescence spectra of the neat and POSS-modified films with SVA and SVA-TA. For all of the films the fluorescence intensity is reduced after thermal annealing, implying more efficient phase separation. The Ph-POSS-modified films show reduced

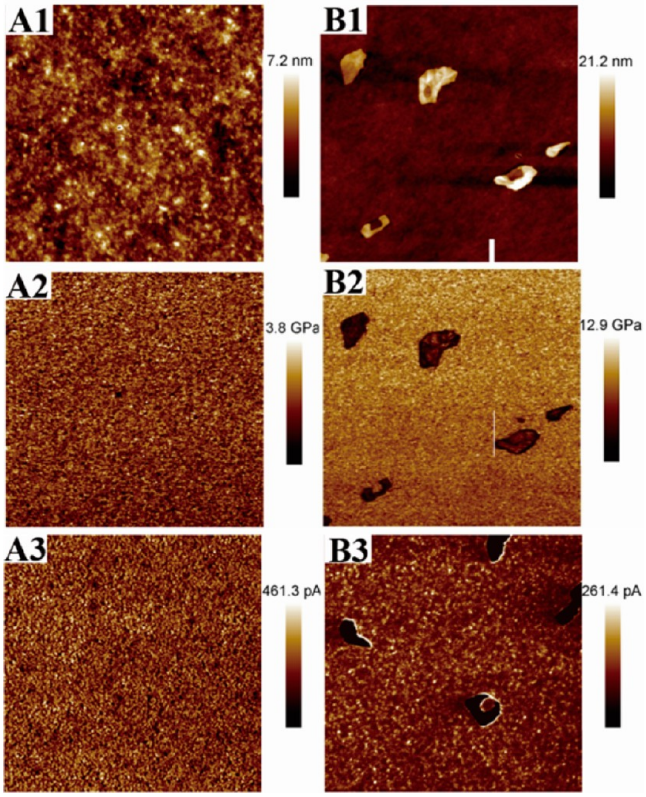

Figure 7. (A1) Height image, (A2) corresponding DMT modulus image, and (A3) current image of the Ph-POSS-modified film after SVA; (B1) height image, (B2) corresponding DMT modulus image, and (B3) current image of the SH-POSS-modified film after SVA. The scale of all images is 5 μm × 5 μm.

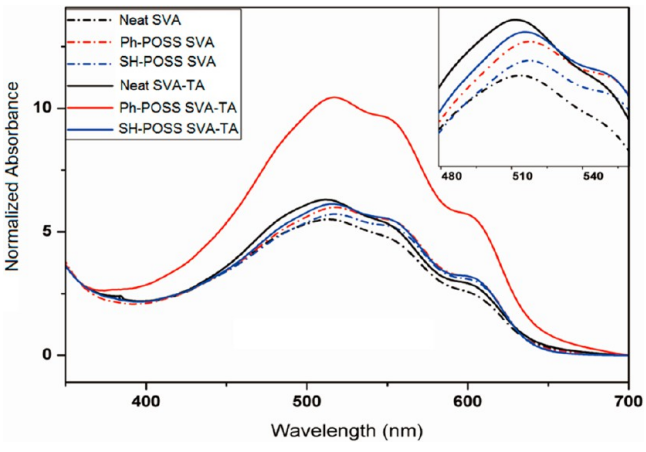

Figure 8. UV–vis spectra of the neat P3HT:PCBM film, the SH-POSS-modified film, and the Ph-POSS-modified film with SVA and SVA-TA.

fluorescence intensity in comparison to the neat film, while the SH-POSS-modified films show increased fluorescence intensity. This indicates that Ph-POSS enhances phase separation and charge transfer, while the SH-POSS reduces efficiency of phase separation. The integrated areas of the spectra between 600 and 800 nm were calculated and tabulated in table 2. Assuming that lower values correspond to better quenching and phase separation, the efficiency trend is Ph-POSS SVA-TA> Neat SVA-TA > Ph-POSS SVA > SH-POSS SVA-TA> Neat SVA > SH-POSS SVA.

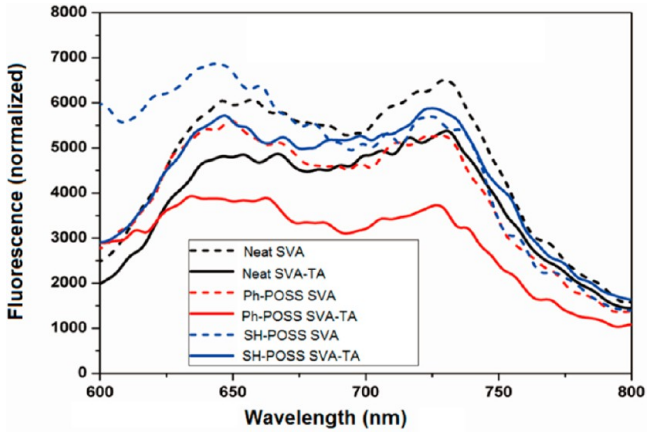

Figure 9. Fluorescence spectra of neat P3HT:PCBM, SH-POSS-modified, and Ph-POSS-modified films with SVA and SVA-TA.

Table 2. Integrated Area ($\times 10^{-4}$) of the Normalized Fluorescence Spectra from 600 to 800 nm

neat SVA	neat SVA-TA	Ph-POSS SVA	Ph-POSS SVA-TA	SH-POSS SVA	SH-POSS SVA-TA
93	78	81	59	96	87

Performance of Solar Cells. Current–voltage curves of the OPV devices with and without POSS incorporation after (A) SVA and (B) SVA-TA are shown in Figure 10. Device performance characteristics (short circuit current density (J_{sc}),

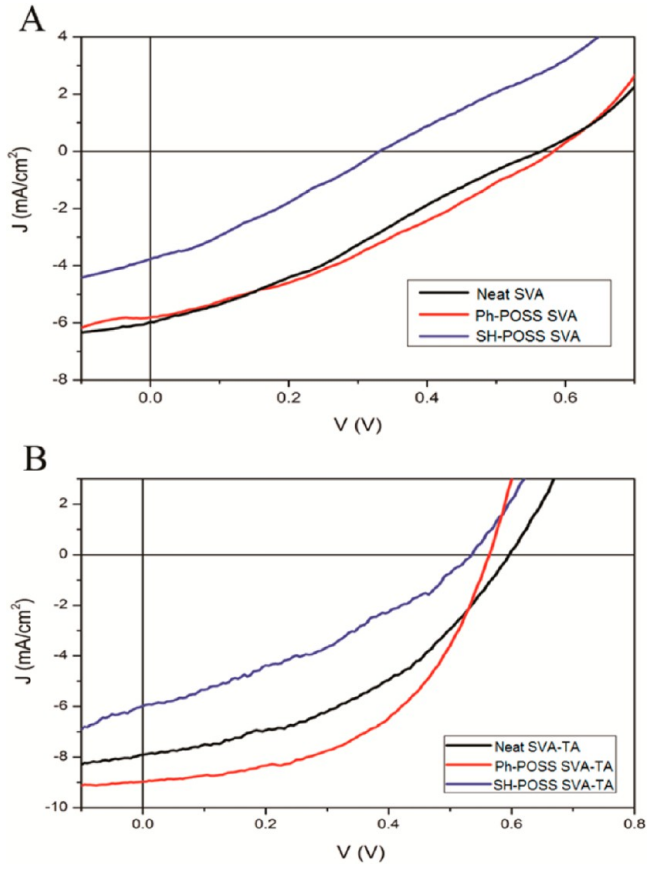

Figure 10. *I–V* curves of (a) devices with only solvent vapor annealing and (b) devices with both solvent vapor and thermal annealing.

dx.doi.org/10.1021/am4010489 | ACS Appl. Mater. Interfaces 2013, 5, 6136–6146

Table 3. Performance of OPV Devices[a]

	J_{sc} (mA/cm^2)	V_{oc} (V)	FF (%)	PCE (%)	R_{sh} (Ω cm^2)	R_s (Ω cm^2)
neat SVA	5.8 ± 0.2	0.57 ± 0.01	32.1 ± 4.0	1.07 ± 0.08	144 ± 49	70 ± 18
neat SVA-TA	7.9 ± 0.2	0.6 ± 0.01	43.9 ± 1.9	2.08 ± 0.10	261 ± 16	29 ± 5
Ph-POSS SVA	5.8 ± 0.3	0.59 ± 0.08	33.4 ± 4.5	1.14 ± 0.13	144 ± 54	81 ± 22
Ph-POSS SVA-TA	9.0 ± 0.3	0.57 ± 0.02	51.2 ± 1.7	2.62 ± 0.13	426 ± 79	13 ± 1
SH-POSS SVA	3.7 ± 0.4	0.33 ± 0.07	29.8 ± 2.2	0.36 ± 0.07	126 ± 41	82 ± 25
SH-POSS SVA-TA	6.0 ± 0.1	0.54 ± 0.04	35.2 ± 2.1	1.14 ± 0.11	144 ± 20	38 ± 8

[a]SVA = isopropanol vapor annealing for 20 min, TA = thermal annealing at 150 °C for 30 min. R_{sh} and R_s are calculated to be equal to the inverse slope at J_{sc} and V_{oc}, respectively. Values presented are averages with ± one standard deviation.

open circuit voltage (V_{oc}), fill factor (FF), power conversion efficiency (PCE), shunt resistance (R_{sh}), and series resistance (R_s) are given in Table 3 (box plot analysis of the data is provided in the Supporting Information, Figure S2). The devices with only SVA show poor performance, with low FF and PCE. Thermal annealing of the neat OPV blend resulted in an increase of the FF from 32.1 to 42.9% and increase of the PCE from 1.07% to 2.08%, attributed to increased phase separation and crystallinity of the P3HT.[52] The addition of Ph-POSS increased the performance while SH-POSS decreased the performance of the cells. Similar trends were observed in J_{sc} as observed in UV−vis absorbance measurements, with the Ph-POSS demonstrating almost 50% improvement in comparison to the SH-POSS system. Absolute levels of improvement were not as high in the device as in the thin films, attributed to device inefficiencies. The thermally annealed Ph-POSS-containing cells exhibited the highest R_{sh}, the lowest R_s and increases in the FF to 51.2% and PCE to 2.62%, in comparison to 43.0 and 2.02%, respectively, for the neat cells. The improvements are attributed to improved phase separation and scattering of the light by the PCBM/POSS clusters into the film, which increases the light absorbance efficiency in the device. Such scattering within the active layer is thought to increase the photon absorption by lengthening the optical path traversed,[49,53] resulting in increased exciton generation. The P3HT/POSS clusters in the SH-POSS-modified films, on the other hand, disrupt thephase-separated morphology, and reduce charge transfer efficiency. It is interesting to note that the measured device efficiency trend follows the same order as that of fluorescence quenching of the films, which indicates that the simpler fluorescence spectroscopy analysis could be used to predict solar cell performance.

Power conversion efficiencies achieved with the incorporation of 1 wt % Ph-POSS are reproducible, statistically significant, and comparable to or greater than those reported with other types of nanoparticles,[10−12,54] where simple incorporation without further treatment often results in a decrease in efficiency. The improvements are also similar to those reported with the addition of PDMS.[22] Addition of high percentages (5−13%) of alkyl thiols yielded greater enhancement of PCE (up to 130% improvement in comparison to 25% improvement for Ph-POSS). These films, however, were twice as thick as our active layers.[24] The promising results reported herein with low weight percentages of POSS materials indicate their potential for further enhancement of device performance, alone or in combination with other additives. The ability to tailor the POSS organic corona with a wide range of specific compositions presents the possibility for compatibility with different photoactive polymeric systems, dispersion of synergistic nanomaterials, and/or introduction of other functionality. Additionally, we suggest that the enhancement in nano-mechanical properties obtained on incorporation of the hybrid POSS nanomaterials may provide an avenue for strengthening and improving the long-term performance of the OPV cells.

4. CONCLUSIONS

Air-processed P3HT:PCBM based photovoltaic films were prepared under both isopropanol solvent vapor annealing alone and SVA combined with thermal annealing. Ph-POSS and SH-POSS were introduced into this system in an attempt to enhance control of the morphology and phase separation. Micron sized aggregates (1−3 μm) were observed in the POSS-modified films after SVA-TA. Raman imaging indicated that the aggregates in the SH-POSS-modified films were rich in P3HT, whereas those observed in the Ph-POSS-modified films had low concentrations of P3HT. Conductive-AFM and nanomechanical mapping demonstrated that the aggregates in the Ph-POSS-modified film exhibited a small amount of conductivity and were of higher relative hardness, providing further evidence of their low P3HT and high Ph-POSS/PCBM content. The aggregates observed in the SH-POSS-modified films, on the other hand, demonstrated low relative hardness and no conductivity, providing further evidence of their higher concentration of P3HT. AFM analysis of the films at different steps in the process indicated that while the SH-POSS/P3HT aggregates formed during solvent vapor annealing, the Ph-POSS/PCBM aggregates did not form until the thermal annealing step. This phenomenon was attributed to the different interactions of the POSS molecules of different structures with the P3HT and PCBM phases; Ph-POSS is expected to interact with the PCBM phase through $\pi-\pi$ interactions, whereas the SH-POSS displays greater interaction with the P3HT phase. UV−vis spectroscopy analysis demonstrated that Ph-POSS incorporation resulted in a doubling of the absorbance in comparison to the neat P3HT:PCBM film, while SH-POSS incorporation reduced absorption. The enhanced light absorption was attributed to improved phase separation and nanoscale morphology in the Ph-POSS containing films and to the Ph-POSS/PCBM aggregates acting as scattering sites to reflect and scatter light within the film. Fluorescence spectroscopy analysis produced a trend of fluorescence quenching in the order of Ph-POSS SVA-TA> Neat SVA-TA > Ph-POSS SVA > SH-POSS SVA-TA> Neat SVA > SH-POSS SVA. Laboratory-scale photovoltaic cells were assembled and their performance analyzed. The Ph-POSS-modified P3HT:PCBM cell exhibited improved performance in comparison to the neat P3HT:PCBM cell, with the short current density increasing from 7.9 to 9.0 mA/cm^2, the fill factor increasing from 43.9 to 51.2% and the power conversion efficiency improving from 2.08 to 2.62%. These improvements were attributed to enhanced phase separation and improved scattering within the film due to Ph-POSS/PCBM aggregates.

The SH-POSS-modified film, on the other hand, showed poorer performance than the standard, which was attributed to greater irregularity in the nanoscale morphology. The trends observed in conductive AFM and fluorescence quenching of the films were the same as those observed in the OPV cells. These findings indicate the promise for improving OPV cell efficiency through incorporation of properly functionalized POSS molecules in phase-separated bulk heterojunction OPV systems.

■ ASSOCIATED CONTENT

Supporting Information

UV−vis absorption curves of Ph-POSS and SH-POSS samples in THF and box plots showing means and variation of the replicate device characteristics data for cells that underwent both SVA and TA. This material is available free of charge via the Internet at http://pubs.acs.org/.

■ AUTHOR INFORMATION

Corresponding Author

*E-mail: Sarah.Morgan@usm.edu.

Author Contributions

†Authors Q.W. and M.B. contributed equally.

Notes

The authors declare no competing financial interest.

■ ACKNOWLEDGMENTS

Funding from The U.S. Department of Energy under grant number DE-EE0003173 and from the Ray C. Anderson Foundation is gratefully acknowledged. The authors thank Hybrid Plastics, Inc., for donation of the POSS materials and for useful discussions.

■ REFERENCES

(1) Xue, J. *Polym. Rev.* **2010**, *50*, 411−419.
(2) Zheng, Y.; Xue, J. *Polym. Rev.* **2010**, *50*, 420−453.
(3) Skotheim, T. A.; Reynolds, J. R., Eds. *Handbook of Conducting Polymers: Conjugated Polymers Processing and Applications*, 3rd ed.; CRC Press, Boca Raton, FL, 2007.
(4) Padinger, F.; Rittberger, R. S.; Sariciftci, N. S. *Adv. Funct. Mater.* **2003**, *13*, 85−88.
(5) Yang, X.; Loos, J.; Veenstra, S. C.; Verhees, W. J. H.; Wienk, M. M.; Kroon, J. M.; Michels, M. A. J.; Janssen, R. A. J. *Nano Lett.* **2005**, *5*, 579−583.
(6) Salamandra, L. *Organic photo-voltaic cells and photo-detectors based on polymer bulk-heterojunctions*. Ph. D. Thesis, University of Rome Tor Vergata, Rome, 2009.
(7) Li, G.; Shrotriya, V.; Huang, J.; Yao, Y.; Moriarty, T.; Emery, K.; Yang, Y. *Nat. Mater.* **2005**, *4*, 864−868.
(8) Hegde, R.; Henry, N.; Whittle, B.; Zang, H.; Hu, B.; Chen, J.; Xiao, K.; Dadmun, M. *Sol. Energy Mater. Sol. Cells* **2012**, *107*, 112−124.
(9) Rider, D. A.; Tucker, R. T.; Worfolk, B. J.; Krause, K. M.; Lalany, A.; Brett, M. J.; Buriak, J. M.; Harris, K. D. *Nanotechnology* **2011**, *22*, 085706/085701−085706/085709.
(10) Berson, S.; de, B. R.; Bailly, S.; Guillerez, S.; Jousselme, B. *Adv. Funct. Mater.* **2007**, *17*, 3363−3370.
(11) Kim, C.-H.; Cha, S.-H.; Kim, S. C.; Song, M.; Lee, J.; Shin, W. S.; Moon, S.-J.; Bahng, J. H.; Kotov, N. A.; Jin, S.-H. *ACS Nano* **2011**, *5*, 3319−3325.
(12) Topp, K.; Borchert, H.; Johnen, F.; Tunc, A. V.; Knipper, M.; von, H. E.; Parisi, J.; Al-Shamery, K. *J. Phys. Chem. A* **2010**, *114*, 3981−3989.
(13) Misra, R.; Fu, B. X.; Plagge, A.; Morgan, S. E. *J. Polym. Sci., Part B: Polym. Phys.* **2009**, *47*, 1088−1102.
(14) Misra, R.; Fu, B. X.; Morgan, S. E. *J. Polym. Sci., Part B: Polym. Phys.* **2007**, *45*, 2441−2455.
(15) Abad, M. J.; Barral, L.; Fasce, D. P.; Williams, R. J. J. *Macromolecules* **2003**, *36*, 3128−3135.
(16) Wheeler, P. A.; Misra, R.; Cook, R. D.; Morgan, S. E. *J. Appl. Polym. Sci.* **2008**, *108*, 2503−2508.
(17) Lligadas, G.; Ronda, J. C.; Galia, M.; Cadiz, V. *Biomacromolecules* **2006**, *7*, 3521−3526.
(18) Misra, R.; Fu, B. X.; Plagge, A.; Morgan, S. E. *J. Polym. Sci., Part B: Polym. Phys.* **2009**, *47*, 1088−1102.
(19) Misra, R.; Alidedeoglu, A. H.; Jarrett, W. L.; Morgan, S. E. *Polymer* **2009**, *50*, 2906−2918.
(20) Xiao, S.; Nguyen, M.; Gong, X.; Cao, Y.; Wu, H.; Moses, D.; Heeger, A. J. *Adv. Funct. Mater.* **2003**, *13*, 25−29.
(21) Lee, R.-H.; Lai, H.-H. *Eur. Polym. J.* **2007**, *43*, 715−724.
(22) Graham, K. R.; Mei, J.; Stalder, R.; Shim, J. W.; Cheun, H.; Steffy, F.; So, F.; Kippelen, B.; Reynolds, J. R. *ACS Appl. Mater. Interfaces* **2011**, *3*, 1210−1215.
(23) Dang, M. T.; Hirsch, L.; Wantz, G.; Wuest, J. D. *Chem. Rev.* **2013**, *113*, 3734−3765.
(24) Ouyang, J.; Xia, Y. *Sol. Energy Mater. Sol. Cells* **2009**, *93*, 1592−1597.
(25) Pivrikas, A.; Stadler, P.; Neugebauer, H.; Sariciftci, N. S. *Org. Electron.* **2008**, *9*, 775−782.
(26) Riisness, I.; Carach, C.; Gordon, M. J. *Appl. Phys. Lett.* **2012**, *100*, 073308/073301−073308/073304.
(27) Huang, Y.-C.; Liao, Y.-C.; Li, S.-S.; Wu, M.-C.; Chen, C.-W.; Su, W.-F. *Sol. Energy Mater. Sol. Cells* **2009**, *93*, 888−892.
(28) Lofaj, F.; Ferdinandy, M.; Cempura, G.; Dusza, J. *J. Eur. Ceram. Soc.* **2012**, *32*, 2043−2051.
(29) Adamcik, J.; Lara, C.; Usov, I.; Jeong, J. S.; Ruggeri, F. S.; Dietler, G.; Lashuel, H. A.; Hamley, I. W.; Mezzenga, R. *Nanoscale* **2012**, *4*, 4426−4429.
(30) Dante, M.; Peet, J.; Nguyen, T.-Q. *J. Phys. Chem. C* **2008**, *112*, 7241−7249.
(31) Derjaguin, B.; Muller, V.; Toporov, Y. P. *J. Colloid Interface Sci.* **1975**, *53*, 314−326.
(32) Butt, H.-J.; Cappella, B.; Kappl, M. *Surf. Sci. Rep.* **2005**, *59*, 1−152.
(33) Watanabe, J.; Lepoutre, P. *J. Appl. Polym. Sci.* **1982**, *27*, 4207−4219.
(34) Zhao, Y.; Xie, Z.; Qu, Y.; Geng, Y.; Wang, L. *Appl. Phys. Lett.* **2007**, *90*, 043504/043501−043504/043503.
(35) Bhattacharya, M.; Wu, Q.; Morgan, S. E. *Polym. Prepr.* **2012**, *53*, 117−118.
(36) Machui, F.; Abbott, S.; Waller, D.; Koppe, M.; Brabec, C. J. *Macromol. Chem. Phys.* **2011**, *212*, 2159−2165.
(37) Nilsson, S.; Bernasik, A.; Budkowski, A.; Moons, E. *Macromolecules* **2007**, *40*, 8291−8301.
(38) Barton, A. F. M. *Chem. Rev.* **1975**, *75*, 731−754.
(39) Park, J. H.; Kim, J. S.; Lee, J. H.; Lee, W. H.; Cho, K. *J. Phys. Chem. C* **2009**, *113*, 17579−17584.
(40) Tsoi, W. C.; James, D. T.; Kim, J. S.; Nicholson, P. G.; Murphy, C. E.; Bradley, D. D. C.; Nelson, J.; Kim, J.-S. *J. Am. Chem. Soc.* **2011**, *133*, 9834−9843.
(41) Klimov, E.; Li, W.; Yang, X.; Hoffmann, G. G.; Loos, J. *Macromolecules* **2006**, *39*, 4493−4496.
(42) Bull, T. A.; Pingree, L. S. C.; Jenekhe, S. A.; Ginger, D. S.; Luscombe, C. K. *ACS Nano* **2009**, *3*, 627−636.
(43) Dennler, G.; Lungenschmied, C.; Neugebauer, H.; Sariciftci, N. S.; Labouret, A. *J. Mater. Res.* **2005**, *20*, 3224−3233.
(44) Dennler, G.; Scharber, M. C.; Brabec, C. J. *Adv. Mater.* **2009**, *21*, 1323−1338.
(45) Natori, I.; Natori, S.; Kanasashi, A.; Tsuchiya, K.; Ogino, K. *J. Polym. Sci., Part B: Polym. Phys.* **2013**, *51*, 368−375.
(46) Garcia, R. J. L.; Parra, A.; Aleman, J. *Green Chem.* **2008**, *10*, 706−711.
(47) Dintcheva, N. T.; Morici, E.; Arrigo, R.; La Mantia, F.; Malatesta, V.; Schwab, J. *eXPRESS Polym. Lett.* **2012**, *6*, 561−571.

(48) Chang, Y.-M.; Wang, L. *J. Phys. Chem. C* **2008**, *112*, 17716−17720.
(49) Garnett, E.; Yang, P. *Nano Lett.* **2010**, *10*, 1082−1087.
(50) Xie, Y.; Bao, Y.; Du, J.; Jiang, C.; Qiao, Q. *Phys. Chem. Chem. Phys.* **2012**, *14*, 10168−10177.
(51) Kim, H.; So, W.-W.; Moon, S.-J. *J. Korean Phys. Soc.* **2006**, *48*, 441−445.
(52) Erb, T.; Zhokhavets, U.; Gobsch, G.; Raleva, S.; Stühn, B.; Schilinsky, P.; Waldauf, C.; Brabec, C. J. *Adv. Funct. Mater.* **2005**, *15*, 1193−1196.
(53) Tan, B.; Wu, Y. *J. Phys. Chem. B* **2006**, *110*, 15932−15938.
(54) Derbal-Habak, H.; Bergeret, C.; Cousseau, J.; Nunzi, J. *Sol. Energy Mater. Sol. Cells* **2011**, *95*, S53−S56.